Chinese Chemical Letters 34 (2023) 108186

Contents lists available at ScienceDirect

Chinese Chemical Letters

journal homepage: www.elsevier.com/locate/cclet

Embedding antimony nanoparticles into metal–organic framework derived TiO_2@carbon nanotablets for high-performance sodium storage

Tianhao Yao[a], Li Li[a,b,*], Hongkang Wang[a,*]

[a] State Key Lab of Electrical Insulation and Power Equipment, Center of Nanomaterials for Renewable Energy (CNRE), School of Electrical Engineering, Xi'an Jiaotong University, Xi'an 710049, China
[b] School of Automotive and Traffic Engineering, Jiangsu University of Technology, Changzhou 213001, China

ARTICLE INFO

Article history:
Received 13 October 2022
Revised 3 November 2022
Accepted 31 January 2023
Available online 2 February 2023

Keywords:
Sodium-ion batteries
Sb/TiO_2
Metal–organic framework
Electrochemical properties
Sodium storage behavior

ABSTRACT

Titanium dioxide (TiO_2) has been widely investigated as a candidate for anode materials of sodium-ion batteries (SIBs) due to its low cost and high abundance. However, the intrinsic sluggish ion/electron transfer rate hinders its practical applications for high energy density storage devices. In contrast, antimony (Sb) shows high specific theoretical capacity (660 mAh/g) as well as excellent electron conductivity, but the large volume variation upon cycling usually leads to severe capacity fading. Herein, with the objective of achieving high-performance sodium storage anode materials, TiO_2@C-Sb nanotablets with a small amount of Sb content (6.4 wt%) are developed through calcination Ti-metal–organic framework (MIL-125) derived TiO_2@C/$SbCl_3$ mixture under reductive atmosphere. Benefitting from the synergetic effect of well-dispersed Sb nanoparticles as well as robust porous TiO_2@C substrate, the TiO_2@C-Sb shows enhanced electron/ion transfer rate and predominantly pseudocapacitive sodium storage behavior, delivering a reversible capacity of 219 mAh/g at 0.5 A/g even after 1000 cycles. More significantly, this method may be commonly used to incorporate other alloy-based high-theoretical materials into MIL-125-derived TiO_2@C, which is promising for developing high-energy-density TiO_2-based energy storage devices.

To address the acute energy crisis and environmental pollution issues created by the usage of fossil fuels, the conversion and exploitation of renewable energy have received considerable attention [1–3]. However, the unstable and unpredictable characteristics of such resources place a premium on energy storage devices with high power/energy density [4]. Lithium-ion batteries (LIBs) have dominated the energy storage market for decades due to their high energy density and long lifespan; however, issues such as limited lithium resources, potential safety problems and high cost impede the development of LIBs for large-scale high power/energy density applications [5–8]. Alternatively, sodium-ion batteries (SIBs) have risen to prominence due to their low cost, abundance, and similar functioning mechanism to LIBs [9,10]. Unfortunately, the traditional anode material for LIBs, graphite, shows limited capacity in SIBs owing to the larger radius of Na^+, which inspires us to exploit novel anode electrode materials with enhanced Na^+ storage performance [11].

Recently, Ti-based oxide material, titanium dioxide (TiO_2), has been widely investigated as a candidate for anode materials of SIBs due to its low cost, facile production, nontoxic and nearly zero strain upon ion insertion [2,5,12-15]. However, the relatively low theoretical specific capacity, sluggish ion diffusion rate, as well as low conductivity usually lead to limited rate capability (Table S1 in Supporting information), which cannot satisfy the requirements of high power/energy density [16–19]. Engineering rational structures, such as nanosheets, hollow and porous structures, have been considered an effective solution to achieve high specific surface area and good penetration of the electrolyte, thereby shortening ion diffusion path and reducing contact resistance [20–24]. In addition, compositing with carbon materials can also enhance the electrochemical performance of TiO_2 as carbon-based anode materials usually show good rate performance (Table S1) [16,25-27]. Metal–organic frameworks (MOFs) are a series of materials composed of orderly linked metal-ions and organic ligands with abundant nano-sized cavities and tunable pore structures, which are ideal precursors for preparing highly porous metal oxides and carbon matrix [28–34]. Shi *et al.* reported an anatase TiO_2@C composite with porous structure using Ti-MOF (MIL-125) as the precursor, which exhibits excellent electrochemical performance when applied as anode materials for SIBs, delivering a reversible storage capacity

* Corresponding authors.
E-mail addresses: liliorigin@jsut.edu.cn (L. Li), hongkang.wang@mail.xjtu.edu.cn (H. Wang).

https://doi.org/10.1016/j.cclet.2023.108186
1001-8417/

of 148 mAh/g after 500 cycles at 0.5 A/g [35]. Recently, many researchers have been looking for other strategies to improve the sodium storage capacity of TiO_2. For example, Wang's group introduced defects to TiO_2/C composite by a facile magnesium reduction, which enhanced electronic and ionic transferability, achieving high-rate performance (172.2 mAh/g at 1 A/g) [36]. Vanadium (V)-doped MIL-125 nanotablets were also prepared by a modified solvothermal method in our previous work. The derived V-doped TiO_2@C nanotablets show improved electric conductivity and ion diffusivity, delivering a reversible capacity of 177 mAh/g after 1000 cycles at 0.5 A/g [13]. Though heteroatom doping and defect engineering can effectively improve the intrinsic ion/electron conductivity of TiO_2, the capacity of pristine TiO_2 still cannot meet the requirement of high energy density. Hybridizing with some alloy-type materials, such as antimony (Sb), tin (Sn), and germanium (Ge), cannot only enhance sodium storage capability but also improve the conductivity of the electrode, among which metallic Sb has received considerable interest due to its high theoretical capacity (660 mAh/g) and extraordinary electronic conductivity [37–39]. More importantly, the sodium insertion potential (0.5–0.8 V *vs.* Na/Na^+) of Sb is close to that of TiO_2 (~0.6 V *vs.* Na/Na^+), which will not introduce extra plateaus [40]. Nevertheless, the huge volume variation caused by the sodiation/desodiation will result in the pulverization of the active materials, thereby leading to severe capacity fading upon cycles (Table S1).

Herein, in order to further improve the sodium storage capacity and meanwhile maintain the cycling stability of MIL-125 derived TiO_2@C, we introduced a small amount of Sb through adsorption by TiO_2@C. After the subsequent calcination under reductive atmosphere, the $SbCl_3$ species were converted to Sb nanoparticles, which were homogeneously distributed within the TiO_2@C nanotablets. Benefiting from the high theoretical capacity and suitable redox potential (*vs.* Na/Na^+) of Sb as well as robust TiO_2@C substrate, the optimized TiO_2@C-Sb shows enhanced sodium storage capacity without additional redox plateaus, delivering a reversible capacity of 219 mAh/g at 0.5 A/g even after 1000 cycles. More importantly, this strategy may also be commonly applied for integrating other alloy-based materials within MIL-125-derived TiO_2@C, which is promising for developing high-energy-density TiO_2-based energy storage devices.

The synthesis route of TiO_2@C-1Sb is schematically illustrated in Fig. 1a. Firstly, MIL-125 was prepared by stirring solvothermal method, where the titanium tetraisopropanolate (TTIP) and *p*-phthalic acid (PTA) serve as Ti source and organic linker, respectively. Secondly, the as-prepared MIL-125 was carbonized under inert atmosphere, during which the Ti^{4+} was *in situ* converted to TiO_2 and meanwhile, the porosity feature of MIL-125 is well inherited. The Sb species were then introduced by mixing the porous TiO_2@C nanotablets with $SbCl_3$/ethanol solution with different concentrations (0.1 and 0.2 mol/L). After calcination under hydrogen, the $SbCl_3$ was successfully converted to metallic Sb nanoparticles within the TiO_2@C nanotablets. For better illustration, the final products, TiO_2@C-Sb, prepared with 0.1 and 0.2 mol/L $SbCl_3$/ethanol solution were denoted as TiO_2@C-1Sb and TiO_2@C-2Sb, respectively.

As revealed in Fig. S1a (Supporting information), the MIL-125 prepared by stirring solvothermal method shows identical X-ray diffraction (XRD) patterns with calculated MIL-125 and typical nanotablet morphology (Figs. S1b and c in Supporting information) with diameters ranging from 200 nm to 600 nm, and thickness of ~300 nm, suggesting the successful synthesis of MIL-125. In the subsequent calcination process, the MIL-125 was converted to TiO_2@C as revealed by XRD (Fig. 1b), where the four typical diffraction peaks at 25.3°, 37.8°, 48.2° and 55.1° well correspond to the (101), (004), (200) and (211) planes of anatase TiO_2 (JCPDS No. 21-1272). The weak diffraction intensity indicates the low crystallization of TiO_2. After the introduction of Sb species, the TiO_2@C-1Sb shows two newly emerged peaks at 28.9° and 42.1°, corresponding to the (012) and (110) planes of Sb (JCPDS No. 35-0732); meanwhile, the diffraction intensity of TiO_2 is weakened possibly due to the acid generated by the hydrolysis of $SbCl_3$ corroding TiO_2 nanoparticles. As the amount of $SbCl_3$ doubled, the TiO_2@C-2Sb showed much stronger diffraction peaks for Sb, indicating that the Sb nanoparticles became larger while the crystallization of TiO_2 remained the same. The enlargement of Sb nanoparticles may be related to that the high-concentration $SbCl_3$ is more prone to agglomeration during drying, thereby forming a larger crystal size. Furthermore, Raman spectra were also used to help confirm the structural phase of TiO_2 and carbon. As shown in Fig. S2 (Supporting information), the peak located at 154 cm^{-1} corresponds to the vibration of Ti-O bonds, while the other two prominent peaks at 1349 and 1599 cm^{-1} are typically attributed to the D-band and G-band of carbon [41]. The intensity ratio of the two latter peaks, I_D/I_G, reflects the disordered degree of carbon, and all these samples show I_D/I_G values of ~0.96, suggesting graphite dominated structure, which will be in favor of electron transfer within the nanotablets [42]. Note that the typical peaks for metallic Sb cannot be observed due to its ultrasmall size as well as low content.

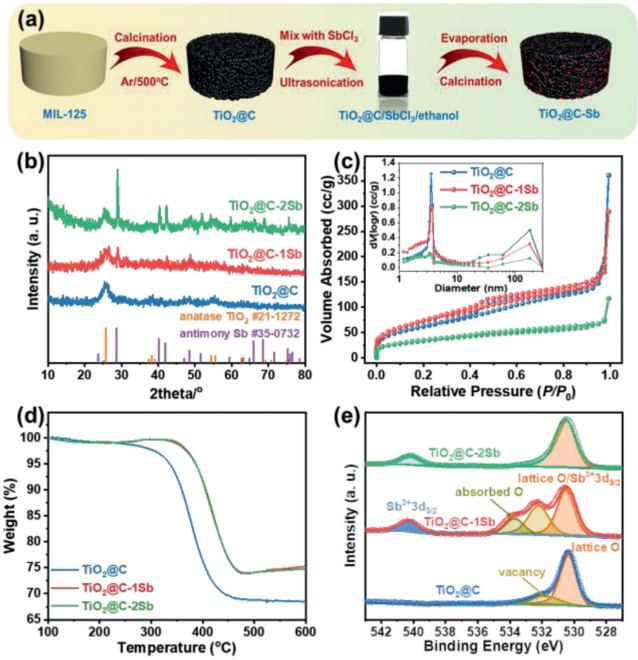

Fig. 1. (a) Schematical illustration of the synthesis of TiO_2@C-Sb. (b) XRD, (c) N_2 sorption isotherms and pore size distribution, (d) TGA curves and (e) Sb 3d/O 1s XPS spectra for TiO_2@C and TiO_2@C-1/2Sb.

The specific surface area of TiO_2@C nanotablets analyzed by the Brunauer–Emmett–Teller (BET) method (Fig. 1c) is ~216.68 m^2/g. Such a high value is attributed to the highly porous structure inherited from the precursor. After introducing Sb species, the specific surface area of TiO_2@C-1Sb increases to 253.86 m^2/g, as the Sb nanoparticles offer more exposed areas. However, as the amount of $SbCl_3$ further increases, the area drops to 116.70 m^2/g for TiO_2@C-2Sb Such a decrease in surface area can be explained by the larger Sb nanoparticles crystallizing on the surface and blocking the pores of TiO_2@C. The pore size distribution (Fig. 1c) was further analyzed through the Barrett-Joyner-Halenda (BJH) method to confirm this. The origin TiO_2@C shows a major pore diameter of 3.5 nm and a total pore volume of 0.577 cc/g. After the Sb species are introduced to the TiO_2@C nanotablets, the pore volume of TiO_2@C-1Sb decreases to 0.481 cc/g, suggesting some Sb nanoparticles are

absorbed into the mesopores of TiO_2@C. As the concentration of the Sb species further increases, the pore volume quickly drops to 0.187 cc/g. Meanwhile, the quantity of pores with a diameter of 3.5 nm also decreases dramatically, confirming the Sb nanoparticles have blocked the pores of TiO_2@C nanotablets.

Thermogravimetric analysis (TGA) was conducted to evaluate the element content. As shown in Fig. 1d, the weight loss before 250 °C of TiO_2@C is related to the removal of absorbed water, and the subsequent weight drop from 300 °C to 500 °C indicates the removal of carbon species, based on which the carbon weight content of TiO_2@C is calculated as 30.2 wt%. As for TiO_2@C-Sb, there is a slight weight rise at 300 °C, corresponding to the surface oxidation of metallic Sb. Interestingly, the TiO_2@C-Sb shows a weight climb above 500 °C, which corresponds to the continuous oxidation of Sb to Sb_2O_3. Consequently, the weight contents of Sb in TiO_2@C-1Sb and TiO_2@C-2Sb are calculated to be 6.4 wt% and 6.1 wt%, respectively. The Sb contents of the TiO_2@C-Sb samples obtained from different concentrations of $SbCl_3$/ethanol solutions are almost the same, while the crystallization is enhanced as the concentration increases, which indicates that (1) the content of absorbed Sb is determined by the material itself, independent of the concentration; (2) the excess $SbCl_3$ remains on the glass breaker wall instead of TiO_2@C nanotablets; (3) higher concentration will result in large crystal size of Sb as evidenced by XRD and pore size distribution. These results suggest that the $SbCl_3$/ethanol solution can be used multiple times as long as the concentration is controlled, thus further reducing the cost of large-scale synthesis.

X-ray photoelectron spectroscopy (XPS) was measured to examine the chemical valence of the samples. The survey XPS spectrum (Fig. S3a in Supporting information) for TiO_2@C confirms the coexistence of C, O and Ti elements. After the incorporation with Sb species, a newly emerged peak at ~540 eV can be observed, corresponding to Sb3d. As shown in Fig. 1e, the O 1s XPS spectrum for pristine TiO_2@C can be deconvoluted into two peaks at 530.3 and 532.0 eV, corresponding to the lattice O and oxygen vacancy, respectively [24,43-45]. After the introduction of Sb, the TiO_2@C-1Sb shows two newly emerged peaks at 533.8 and 540.2 eV, which can be indexed to the absorbed O and Sb^{3+} $3d_{3/2}$ [42,46-48]. Note that the peak of Sb^{3+} $3d_{5/2}$ can hardly be detected because it overlaps with lattice O. The Sb^0, however, cannot be observed in the spectrum due to the surface oxidation of Sb, which is inevitable when exposed to air. The peak for oxygen vacancy becomes much more prominent in TiO_2@C-1Sb due to thermal annealing under hydrogen atmosphere, leading to reduction of TiO_2 nanoparticles. As for TiO_2@C-2Sb, the peaks of Sb^{3+} and lattice O can still be observed, while the peak for oxygen vacancy is missing, suggesting that the Sb particles are so large that they cover the TiO_2 part. Furthermore, the Ti2p XPS spectra for the samples are also available in Fig. S3b (Supporting information), where the peaks at 459.0 and 464.8 eV in the TiO_2@C can be well indexed to the Ti^{4+} $2p_{3/2}$ and $2p_{1/2}$ [49,50]. After calcination under reductive atmosphere, these two peaks show shifts to lower binding energy, suggesting the emergence of Ti^{3+} species, which is in good agreement with the appearance of oxygen vacancies in TiO_2@C-1Sb [13,51].

The morphology feature and microstructure were then analyzed by scanning electron microscope (SEM) and transmission electron microscope (TEM). The pristine TiO_2@C maintains its nanotablets morphology after calcination (Fig. 2a *vs.* Fig. S1 in Supporting informaiton). As shown in Fig. S4 (Supporting informaiton), the TiO_2@C nanotablet is composed of numerous nanoparticles, forming a highly porous structure. A high-resolution TEM (HRTEM, Fig. S4b) image taken at the edge of the nanotablets shows that the nanoparticles are composed of TiO_2 with a lattice spacing of 0.352 nm, well corresponding to the (101) planes of anatase TiO_2 (JCPDS No. 21-1272). The high-angle annular dark-field scanning transmission electron microscopy (HAADF-STEM) image (Fig. S4c)

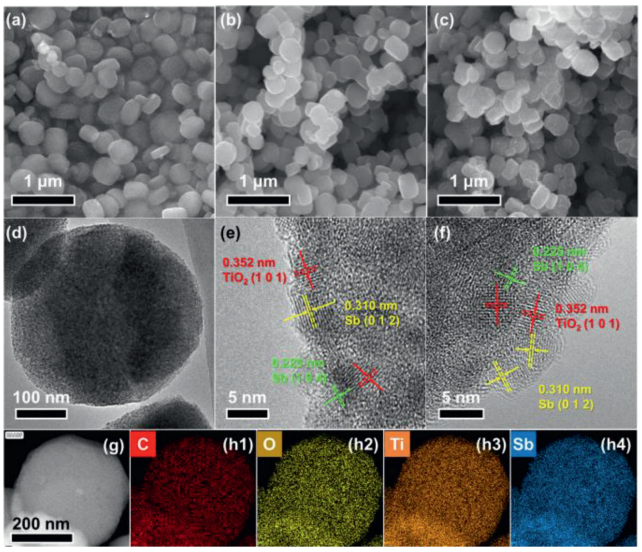

Fig. 2. (a-c) SEM images of (a) TiO_2@C, (b) TiO_2@C-1Sb and (c) TiO_2@C-2Sb (d) TEM image of TiO_2@C-1Sb and HRTEM images of (e) TiO_2@C-1Sb and (f) TiO_2@C-2Sb (g) HAADF-STEM image and (h) corresponding elemental maps for TiO_2@C-1Sb.

and corresponding maps (Fig. S4d) illustrate that the C, O and Ti elements are homogeneously dispersed within the nanotablets. After introducing Sb species, the TiO_2@C-1Sb (Fig. 2b) shows similar morphology to the pristine TiO_2@C nanotablets, while the surface of TiO_2@C-2Sb nanotablets (Fig. 2c) becomes rough, which is due to the agglomeration of Sb on the surface of nanotablets. As observed in Fig. 2d, the TiO_2@C-1Sb inherited its porous morphology after integration with Sb. On the contrary, the TiO_2@C-2Sb (Fig. S5a in Supporting information) becomes less smooth, and some nanoparticles can be seen growing on the outside of the nanotablets. To confirm their microstructures, HRTEM images were also taken (Figs. 2e and f). As for TiO_2@C-1Sb, three clear lattice fringes with different spacing of 0.352, 0.310 and 0.225 nm, corresponding to the (101) planes of TiO_2, (012) and (104) planes of Sb, can be detected within the nanotablets, which suggests that the metallic Sb nanoparticles are successfully embedded into the TiO_2@C nanotablets. The same lattice fringes can also be observed in TiO_2@C-2Sb, however, the Sb nanoparticles grow on the outside of the TiO_2@C nanotablets and with larger size, which well explains its rough surface as seen in Fig. 2c. Furthermore, the HAADF-STEM image (Fig. 2g and Fig. S5b in Supporting information) and corresponding maps (Fig. 2h and Fig. S5c in Supporting information) confirm the homogeneous distribution of C, O, Ti and Sb elements in TiO_2@C-1/2Sb The SEM and TEM results demonstrate the Sb species have been successfully absorbed by TiO_2@C nanotablets, however, the higher concentration of $SbCl_3$ will lead to agglomeration of Sb on the surface.

The electrochemical performance of TiO_2@C and TiO_2@C-1/2Sb has been evaluated in half cells, where sodium foil served as both reference and counter electrodes. The initial five cyclic voltammetry (CV) sweeps for the TiO_2@C electrode in the potential range of 0.01–3 V (*vs.* Na/Na^+) are depicted in Fig. S6a (Supporting information), where a broad cathodic peak at 1 V can be observed in the first anodic sweep, corresponding to the formation of solid electrolyte interface (SEI) layer on the surface of the electrode and the reduction of Ti^{4+} to Ti^{3+} [7,13,52]. The following peak at 0.43 V is associated with the irreversible insertion of Na^+ into the carbon substrate [53]. In the following sweeps, there is only one oxidation peak at 0.78 V, which corresponds to the oxidation of Ti^{3+} to Ti^{4+} [54]. The TiO_2@C-1Sb (Fig. 3a) shows a similar shape to that of the TiO_2@C electrode in the first cathodic sweep, except that a

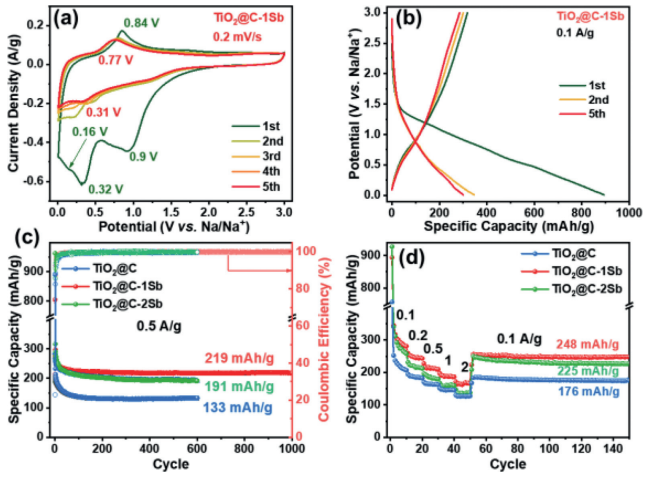

Fig. 3. (a) CV curves and (b) galvanostatic charge–discharge profiles for TiO_2@C-1Sb electrode. (c) Rate and (d) cycling performance for TiO_2@C and TiO_2@C-1/2Sb electrodes.

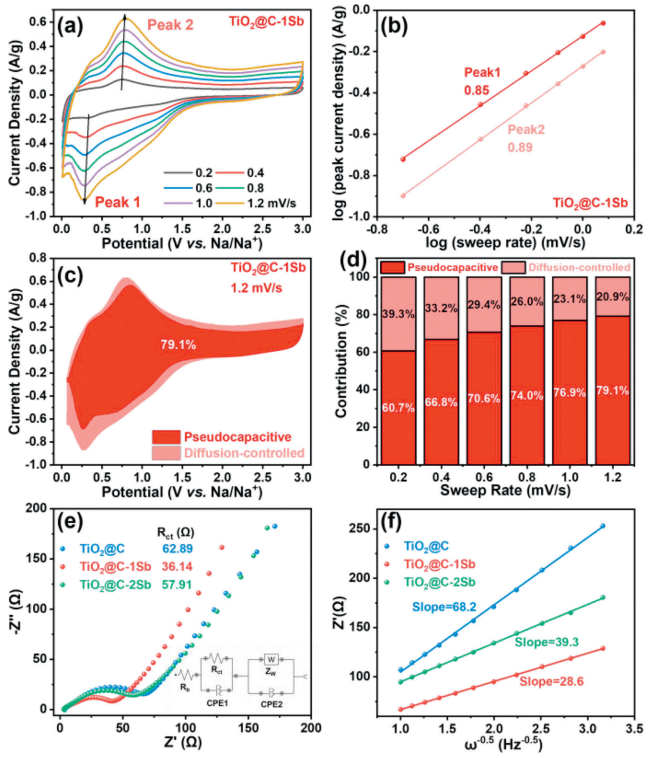

Fig. 4. (a) CV curves with sweep rates of 0.2–1.2 mV/s, (b) corresponding log(peak current) *vs.* log(sweep rate) plots with fitted lines showing the slope value, (c) separation of pseudocapacitive and diffusion-controlled contributions at 1.2 mV/s and (d) pseudocapacitive contribution at different sweep rates for TiO_2@C-1Sb electrode. (e) Nyquist plots with corresponding equivalent circuit (also available in Fig. S10 in Supporting information) and (f) corresponding Z' *vs.* $\omega^{-0.5}$ plots with fitted lines showing slope values for all three electrodes.

new plateau at 0.16 V emerges, which is associated with the alloy reaction of Sb with Na [55,56]. Subsequently, the peak at 0.84 V in the following anodic sweep corresponds to the dealloying process from Na_3Sb to Sb accompanied by the oxidation of Ti^{3+} to Ti^{4+} [57]. In the following sweep, the cathodic peak gradually shifts to 0.28 V, while the anodic peak shifts to 0.77 V due to the restructure of the anode material. Interestingly, unlike other Sb-based anode materials [58–60], the typical redox peaks for the multistep transformation between Sb and Na_3Sb cannot be observed due to the ultrasmall Sb particle size in TiO_2@C-1Sb [46]. From the fourth sweep, the CV curves are well overlapped, suggesting its highly reversible sodium storage process. Note that the similar redox potentials of TiO_2 and Sb not only offer extra sodium storage capacity in the low potential but also avoid the emergence of other voltage plateaus, which is crucial in practical applications. The CV curves of TiO_2@C-2Sb are also available in Fig. S6b (Supporting information), which show almost the same shape as that of the TiO_2@C-1Sb electrode.

The galvanostatic charge–discharge profiles at 0.1 A/g of TiO_2@C and TiO_2@C-1/2Sb are shown in Fig. S7 (Supporting information) and Fig. 3b. The pristine TiO_2@C electrode exhibits an initial discharge/charge specific capacity of 215.9/756.9 mAh/g, corresponding to a low initial Columbic efficiency (ICE) of 28.5%. Note that such a low ICE is mainly attributed to the large specific area and highly porous feature derived from MIL-125, which will consume more Na^+ forming SEI film [61]. As for the TiO_2@C-1Sb electrode, two small plateaus at ~1.3 and 0.5 V can be observed in the first discharge profile, corresponding to the reduction of Ti^{4+} accompanied by the formation of SEI film and the irreversible reaction between carbon substrate and Na^+, respectively. The TiO_2@C-1Sb electrode delivers an initial discharge/charge capacity of 893.6/317.9 with a higher ICE of 35.6%. In the following cycles, two main plateaus at 0.4 V (discharge) and 0.75 V (charge) can be observed, which is in good agreement with CV results. The TiO_2@C-2Sb electrode (Fig. S7b) shows similar charge–discharge profiles shape to TiO_2@C-1Sb, delivering an initial discharge/charge capacity of 926.9/310.1 with an ICE of 33.4%.

The cycling performances of the TiO_2@C and TiO_2@C-1/2Sb electrodes are also compared in Fig. 3c, all these three electrodes show capacity fading in the first several cycles, which is related to the reactions between the surface of the TiO_2@C tablets and the electrolyte as well as irreversible trapping of Na^+ at active sites of the carbon matrix [62,63]. Afterwards, the Coulombic efficiency quickly rises to above 99% from the 10th cycle. The pristine TiO_2@C delivers a limited specific capacity of 133 mAh/g after 600 cycles. After incorporating with Sb species, the TiO_2@C-1Sb shows much-improved sodium storage capacity and cycling stability, delivering a reversible specific capacity of 219 mAh/g after 1000 cycles, which are higher than most of other previously reported TiO_2-based anodes (Table S2 in Supporting information). The high sodium storage capacity for TiO_2@C-1Sb mainly originated from the synergetic effect of high theoretical capacity of Sb species as well as the improved electron/ion transferability (will be discussed in electrochemical impedance spectroscopy (EIS) analysis). However, the TiO_2@C-2Sb shows capacity fading upon cycles, maintaining only 191 mAh/g after 600 cycles, which is mainly due to its larger Sb particle size which produces severe volume variation upon cycling. Furthermore, the rate performance was also compared in Fig. 3d, where the TiO_2@C-1Sb electrode delivers capacities of 280.6, 243.1, 209.7, 186.3 and 165.4 mAh/g at 0.1, 0.2, 0.5, 1 and 2 A/g respectively after 10 cycles, when the current reverts to 0.1 A/g, it still maintains a high reversible capacity of 248 mAh/g after another 100 cycles. On the contrary, the TiO_2@C-2Sb electrode suffers from severe capacity loss, only delivering capacities of 259.1, 212.0, 179.8, 159.6 and 137.2 mAh/g under the same condition, as the current drops back to 0.1 A/g, it shows a lower reversible capacity of 225.0 mAh/g after another 100 cycles.

To further unravel the sodium storage behavior and ion diffusion kinetics, CV curves at various sweep rates and EIS measurements have been carried out. Fig. 4a shows the CV curves of the TiO_2@C-1Sb electrode with sweep rates ranging from 0.2 mV/s to 1.2 mV/s, where the characteristic redox peaks show little shift as the sweep rate increases, indicating low polarization of the TiO_2@C-1Sb electrode at high rates. The sodium storage behav-

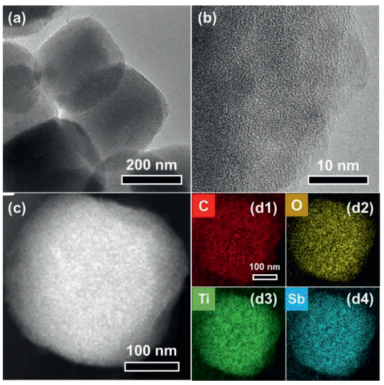

Fig. 5. *Ex situ* (a) TEM, (b) HRTEM, (c) HAADF-STEM images and (d) corresponding maps of charged TiO_2@C-1Sb after 1000 cycles.

ior can be evaluated by fitting the log(peak current)-log(sweep rate), where the slope value reflects whether a diffusion-controlled (slope = 0.5) process or a pseudocapacitive process (slope = 1) dominates the sodium storage behavior [64]. As shown in Fig. 4b, the TiO_2@C-1Sb electrode gives slope values of 0.85 and 0.89, suggesting a pseudocapacitive-dominated sodium storage behavior. Meanwhile, the TiO_2@C-2Sb and pristine TiO_2@C electrode show similar values of 0.81, 0.89 (TiO_2@C-2Sb, Figs. S8c and d in Supporting information) and 0.82 (TiO_2@C, Figs. S8a and b in Supporting information). The pseudocapacitive contribution under each sweep rate for these electrodes is quantitatively calculated and compared and shown in Figs. 4c and d and Fig. S9 (Supporting information) [65]. The pristine TiO_2@C electrode shows a high pseudocapacitive contribution of 75.2% at the sweep rate of 1.2 mV/s. Such a high pseudocapacitive sodium storage behavior is related to its inherent porous structure and high-conductivity carbon matrix derived from MIL-125. Meanwhile, the TiO_2@C-1Sb and TiO_2@C-2Sb give similar pseudocapacitive contributions of 79.1% and 79.5%, respectively, under the same condition.

EIS measurements were also carried out to investigate the electron/ion transfer kinetics in the electrodes. The semi-circle in the high-frequency region of Nyquist plots (Fig. 4e) is related to charge transfer resistance (R_{ct}) [66]. The TiO_2@C-1Sb electrodes show a much lower R_{ct} value (36.14 Ω) than that of the pristine TiO_2@C electrode (62.89 Ω). The TiO_2@C-2Sb, however, shows a high R_{ct} value of 57.91 Ω due to the larger size of Sb nanoparticles. Furthermore, the sodium-ion diffusion kinetics was analyzed based on the inclined line in the low-frequency region, and the detail is also available in Supporting information [13]. The TiO_2@C-1Sb shows an enhanced ion diffusion rate with a low slope value of 28.6 (Fig. 4f), which corresponds to a higher ion diffusion rate, while the TiO_2@C and TiO_2@C-2Sb give slope values of 68.2 and 39.3, respectively. The improved ion transfer rate of TiO_2@C-1Sb can be ascribed to its high specific surface area and ultrasmall Sb particle size, shortening the ion diffusion path.

Ex situ TEM was applied to examine the morphology evolution after cycling. As shown in Fig. 5a, the TiO_2@C-1Sb still maintains its porous nanotablet morphology even after 1000 cycles, and the nanoparticles can be well-defined within the nanotablets. The HRTEM image shown in Fig. 5b illustrates that no obvious lattice finger can be detected after cycles, which can be ascribed to the repeated insertion/extraction of sodium ions damaging its lattice structure. The HAADF-STEM image and corresponding elemental maps are shown in Figs. 5c and d, revealing that the C, O, Ti and Sb are well overlapped without phase separation. These findings further confirm the robust structure stability of the TiO_2@C-1Sb nanotablets during cycling, which well explains the outstanding long-term cycling stability.

In summary, A MOF-derived porous TiO_2@C nanotablet decorated with Sb nanoparticles was developed through absorption and subsequent calcination, where the concentration of the absorption solution ($SbCl_3$/ethanol) only affects the grain size of Sb nanoparticles and their distribution. The optimized product, TiO_2@C-1Sb, exhibits a nanoscale combination configuration with Sb and TiO_2 nanoparticles uniformly scattered within the porous carbon matrix. Benefitting from the synergetic effects of well-dispersed Sb nanoparticles as well as robust TiO_2@C substrate, the TiO_2@C-1Sb shows enhanced sodium storage capacity, delivering a reversible capacity of 219 mAh/g at 0.5 A/g even after 1000 cycles. Further analysis reveals that the TiO_2@C-1Sb electrode also displays predominantly pseudocapacitive sodium storage behavior and improved electron/ion transfer capability. More significantly, this method may be commonly used to incorporate other alloy-based high-theoretical materials into MIL-125-derived TiO_2@C, which is promising for developing high-energy-density TiO_2-based energy storage devices.

Declaration of competing interest

The authors declare that they have no known competing financial interests or personal relationships that could have appeared to influence the work reported in this paper.

Acknowledgments

This work was supported by the National Natural Science Foundation of China (Nos. 52077175, 51905236), the State Key Laboratory of Electrical Insulation and Power Equipment (No. EIPE22204), the Natural Science Research Project of Higher Education Institutions in Jiangsu Province (No. 20KJA480005) and the Qinglan Engineering Project of Jiangsu Universities. We thank Chao Li from the Instrument Analysis Center of Xi'an Jiaotong University for TEM measurements.

Supplementary materials

Supplementary material associated with this article can be found, in the online version, at doi:10.1016/j.cclet.2023.108186.

References

[1] W.B. Yu, W.D. Dong, C.F. Li, et al., J. Energy Chem. 59 (2021) 38–46.
[2] G.R. Wang, Y.P. Li, Y. Liu, et al., Chem. Eng. J. 417 (2021) 127977.
[3] B. Chen, M. Humayun, Y. Li, et al., ACS Sustain. Chem. Eng. 9 (2021) 14180–14192.
[4] Q. Li, H. Wang, X. Tang, et al., Adv. Funct. Mater. 31 (2021) 2101081.
[5] M. Yao, A. Gao, R. Chen, et al., Adv. Mater. Interfaces 9 (2022) 2201140.
[6] H. Wang, T. Yao, C. Li, et al., Chem. Eng. J. 397 (2020) 125385.
[7] D. Zou, W. Wang, J. Liu, et al., Carbon 194 (2022) 248–256.
[8] M. Yang, Z. Sun, P. Nie, et al., Chin. Chem. Lett. 33 (2022) 470–474.
[9] J. Zong, F. Wang, C. Nie, et al., J. Mater. Chem. A 10 (2022) 10651–10661.
[10] Y. Zhou, Y. Liu, M. Zhang, et al., Chem. Eng. J. 433 (2022) 133778.
[11] F. Yang, S. Wang, J. Guan, et al., J. Mater. Chem. A 9 (2021) 27072–27083.
[12] M. Yao, H. Wang, R. Qian, et al., Inorg. Chem. Front. 8 (2021) 5024–5033.
[13] T. Yao, H. Wang, J. Colloid Interface Sci. 604 (2021) 188–197.
[14] P. Gao, H. Shi, T. Ma, et al., ACS Appl. Mater. Interfaces 13 (2021) 51028–51038.
[15] Y. Fang, Y. Zhang, C. Miao, et al., Nano-Micro Lett. 12 (2020) 128.
[16] Z. Le, F. Liu, P. Nie, et al., ACS Nano 11 (2017) 2952–2960.
[17] H. Xu, Y. Liu, T. Qiang, et al., Energy Storage Mater. 17 (2019) 126–135.
[18] H. He, Q. Gan, H. Wang, et al., Nano Energy 44 (2018) 217–227.
[19] M. Wu, Y. Gao, Y. Hu, B. Zhao, H. Zhang, Chin. Chem. Lett. 31 (2020) 897–902.
[20] K. Lan, Y. Liu, W. Zhang, et al., J. Am. Chem. Soc. 140 (2018) 4135–4143.
[21] H. Li, J. Lang, S. Lei, et al., Adv. Funct. Mater. 28 (2018) 1800757.
[22] B. Li, B. Xi, Z. Feng, et al., Adv. Mater. 30 (2018) 1705788.
[23] J. Ni, S. Fu, C. Wu, et al., Adv. Mater. 28 (2016) 2259–2265.
[24] Y. Wu, Y. Jiang, J. Shi, L. Gu, Y. Yu, Small 13 (2017) 1700129.
[25] J. Yin, H. Yang, W. Kong, et al., J. Colloid Interface Sci. 582 (2021) 526–534.
[26] M.N. Tahir, B. Oschmann, D. Buchholz, et al., Adv. Energy Mater. 6 (2016) 1501489.
[27] M. Yao, L. Li, T. Yao, et al., J. Alloys Compd. 926 (2022) 166943.
[28] Z. Wang, X. Li, H. Xu, et al., J. Mater. Chem. A 2 (2014) 12571.

[29] F. Xiao, X. Yang, D. Wang, et al., ACS Appl. Mater. Interfaces 12 (2020) 12809–12820.
[30] F. Xiao, X. Yang, H. Wang, et al., Adv. Energy Mater. 10 (2020) 2000931.
[31] T. Yao, H. Wang, J. Wang, et al., ChemistrySelect 4 (2019) 10576–10580.
[32] X. Xu, Q. Deng, H.C. Chen, et al., Research 2022 (2022) 9837109.
[33] J. Liu, C. Chen, K. Zhang, L. Zhang, et al., Chin. Chem. Lett. 32 (2021) 649–659.
[34] K. Zhang, F. Chu, Y. Hu, et al., Chin. Chem. Lett. 34 (2023) 107766.
[35] X. Shi, Z. Zhang, K. Du, et al., J. Power Sources 330 (2016) 1–6.
[36] H. He, Q. Zhang, H. Wang, et al., J. Power Sources 354 (2017) 179–188.
[37] X. Zhao, S.A. Vail, Y. Lu, et al., ACS Appl. Mater. Interfaces 8 (2016) 13871–13878.
[38] W. Luo, P. Zhang, X. Wang, et al., J. Power Sources 304 (2016) 340–345.
[39] W. Ma, K. Yin, H. Gao, et al., Nano Energy 54 (2018) 349–359.
[40] J. Yang, M. Huang, L. Xu, X. Xia, C. Peng, Chem. Eng. J. 445 (2022) 136638.
[41] T. Wang, Z. Huang, D. Wang, et al., Chin. Chem. Lett. 34 (2023) 107216.
[42] T. Liu, T. Yao, L. Li, et al., J. Colloid Interface Sci. 580 (2020) 21–29.
[43] L. Huang, L. Zeng, J. Zhu, et al., J. Power Sources 493 (2021) 229678.
[44] C. Wang, Y. Tian, Y. Gu, et al., Nano Energy 85 (2021) 106030.
[45] H. Sun, C.W. Tung, Y. Qiu, et al., J. Am. Chem. Soc. 144 (2022) 1174–1186.
[46] A.G. Nguyen, H.T.T. Le, R. Verma, D.L. Vu, C.J. Park, Chem. Eng. J. 429 (2022) 132359.
[47] R. Verma, A.G. Nguyen, P.N. Didwal, et al., Chem. Eng. J. 446 (2022) 137302.
[48] A. Yamuna, T.W. Chen, S.M. Chen, M.C. Yu, J. Yu, Ceram. Int. 48 (2022) 2369–2376.
[49] G. Liu, L. Xu, Y. Li, et al., Chem. Eng. J. 430 (2022) 132689.
[50] Z. Guan, K. Zou, X. Wang, Y. Deng, G. Chen, Chin. Chem. Lett. 32 (2021) 3847–3851.
[51] D. Lv, D. Wang, N. Wang, et al., J. Energy Chem. 68 (2022) 104–112.
[52] R. Wang, S. Wang, Y. Zhang, et al., J. Mater. Chem. A 6 (2018) 1017–1027.
[53] C. Xu, X. Kou, B. Cao, H.T. Fang, Electrochim. Acta 355 (2020) 136782.
[54] Y. Song, Y. Peng, H. Li, et al., Chem. Eng. J. 447 (2022) 137450.
[55] L. Ji, W. Zhou, V. Chabot, A. Yu, X. Xiao, ACS Appl. Mater. Interfaces 7 (2015) 24895–24901.
[56] S. Qiu, X. Wu, L. Xiao, et al., ACS Appl. Mater. Interfaces 8 (2016) 1337–1343.
[57] H. Gao, J. Niu, C. Zhang, Z. Peng, Z. Zhang, ACS Nano 12 (2018) 3568–3577.
[58] H. Hou, M. Jing, Y. Yang, et al., J. Power Sources 284 (2015) 227–235.
[59] H. Hou, M. Jing, Y. Yang, et al., ACS Appl. Mater. Interfaces 6 (2014) 16189–16196.
[60] L. Hu, X. Zhu, Y. Du, et al., Chem. Mater. 27 (2015) 8138–8145.
[61] N.T. Aristote, K. Zou, A. Di, et al., Chin. Chem. Lett. 33 (2022) 730–742.
[62] S. Brutti, V. Gentili, H. Menard, B. Scrosati, P.G. Bruce, Adv. Energy Mater. 2 (2012) 322–327.
[63] C. Chen, Y. Wen, X. Hu, et al., Nat. Commun. 6 (2015) 6929.
[64] H. Gu, R. Zhang, P. Wang, J. Colloid Interface Sci. 533 (2019) 445–451.
[65] F. Xiao, X. Yang, H. Wang, ACS Appl. Mater. Interfaces 12 (2020) 54644–54652.
[66] T. Yao, M. Yao, H. Wang, Sustain. Energy Fuels 6 (2022) 822–833.